Elasticity of carbon allotropes. IV. Rhombohedral graphite: Elasticity, zone-center optic modes, and phase transformation using transferred Keating parameters

C. S. G. Cousins
School of Physics, University of Exeter, Stocker Road, Exeter EX4 4QL, United Kingdom
(Received 10 May 2002; published 22 January 2003)

Early work indicates that this never-isolated ''allotrope'' is a mosaic distribution of microcrystalline defect regions embedded in a hexagonal graphite host. These regions are nevertheless large enough to merit treating rhombohedral graphite as a true allotrope. A modified Keating model is set up and full sets of partial and inner elastic constants at both second and third order are obtained in terms of the Keating parameters. When the parameters derived for hexagonal graphite are used the resulting elastic constants are very similar. Small differences are due to the lower symmetry of the rhombohedral material and the consequently greater number of internal strain components. The single major difference is in the in-plane anharmonic compressibility which is 5.8 TPa^{-2} for the hexagonal material but -30.5 TPa^{-2} for the rhombohedral. The two zone-center optic-mode frequencies and their pressure derivatives match precisely two of the hexagonal modes. A pressure-induced phase transition is indicated at around 22 GPa. A simple switching function is used to interpolate between rhombohedral graphite and cubic diamond parameter sets enabling the proposed transition between those structures to be explored in detail. A degeneracy of the optic-mode frequencies is found in the transition region when the axial bond has a length of 1.9 Å . This corresponds to the symmetry-imposed level crossing at the Γ point associated with the transition from sp^2+p_z to sp^3 bonding. Hydrostatic and other compression paths are also discussed.

DOI: 10.1103/PhysRevB.67.024110 PACS number(s): 62.20.Dc, 63.20.−e

I. INTRODUCTION

In Paper II of this sequence[1] the modified Keating parameters deduced for cubic diamond (cD) in Paper I (Ref. 2) were transferred to hexagonal diamond (hD) with success, judging by the satisfactory prediction of the few experimental data available. In the same spirit the Keating parameters deduced for hexagonal graphite (hG) in Paper III (Ref. 3) will be used to discuss rhombohedral graphite (rG) about which very little is known experimentally.

There are several theoretical studies in the literature: band-structure studies by Haering,[4] theoretical investigations of the rG-to-cD conversion by Kertesz and Hoffmann,[5] and Fahy *et al.*,[6] and comparative *ab initio* studies of a number of forms of graphite by Charlier *et al.*[7] All refer to the fact that rG has never been isolated and state that it constitutes from 5 to 15% of most naturally occurring graphite. Since an allotrope is defined as a *distinct crystalline form* of an element it is possible that rG may not be a genuine allotrope but that there is nevertheless *something* whose nature is worthy of study. A clearer idea of what that is may be inferred from the original structure investigations.

II. DOES THE RHOMBOHEDRAL ALLOTROPE EXIST?

The earliest work is that of Lipson and Stokes[8] who were led to study an x-ray powder photograph of arc-crystallized graphite in order to elucidate some faint lines that could not be explained by the accepted structure of hG.[9–11] Such lines had been found quite generally in photographs from a wide variety of natural and artificial specimens. When they were indexed on the basis of a hexagonal cell they were found to have simple fractional ℓ indices that were always multiples of $\frac{2}{3}$. The simplest explanation was a structure with a unit cell whose c parameter was $\frac{3}{2}$ times the usual one mixed in with the ordinary one. Careful measurements of the intensities of all the lines showed that some had contributions from both structures, some were unique to the hexagonal form and some to the rhombohedral. Quantitatively, however, the enhancement of the intensities of the common lines was not quite right and Lipson and Stokes attempted to remove the new structure by digestion with concentrated sulphuric and nitric acids. The faint lines were removed but the enhanced lines were as enhanced as before. They concluded, first, that the action of the acid had been to rearrange the layers of atoms rather than to remove the new structure, a view supported by the broadening of lines with ℓ nonzero (the regular arrangement of layers had been disturbed) and the unchanged width of lines with ℓ zero (the integrity of planar layers had been preserved) and, second, that there would always be a proportion of disordered material. All the intensity data would be consistent if their sample comprised 14% of the rhombohedral, 80% of the hexagonal, and 6% of the disordered structures. The structure they proposed for rG has $a=2.456$ Å, $c=10.044$ Å, and $u=\frac{1}{6}$. They also stated that the value $u=0.164$ would give slightly better agreement with the observed x-ray intensities. This point is taken up later.

The other major study is that of Freise and Kelly[12] who deformed natural graphite single crystals and polycrystals at room temperature and coupled optical and electron-microscopic investigations of these with x-ray investigations of the appearance and disappearance of the peaks corresponding to the rhombohedral form. Before detailing their own experiments they summarized earlier work on the dislocation structure of natural graphite: all total dislocations are observed to have Burgers vectors of the type $a/3\langle 11\bar{2}0\rangle$. In addition these dislocations are observed to split into par-

tial dislocations with Burgers vectors of the type $a/3\langle 1\bar{1}00\rangle$. In a graphite crystal with the layer planes arranged in the hexagonal stacking sequence, the associated stacking fault becomes a region arranged in the rhombohedral stacking sequence. They report values of the stacking-fault energy centered on 0.55 erg/cm^2,[13,14] equivalent to 0.09 meV per atom in the plane.

Their first experiment showed that their starting material, both single-crystal and polycrystalline samples, had no rhombohedral component. Next they compressed their single crystals along the *c* axis between not-quite-parallel platens. This axial loading was necessary to enable shear to be applied in the basal plane without wholesale cleavage. No rhombohedral form was induced by shear. However, when they took filings from the single crystal, a process that involves much greater shear deformation, a large fraction of the rhombohedral form was detected. Extensive annealing studies were then carried out to characterize the rhombohedral domains. Directly after deformation they were about ten layers thick. With increasing annealing temperature both the thickness of the domains and the volume fraction of the rhombohedral material decreased. The annealing behavior is independent of time at a particular temperature, indicating that the disappearance of the rhombohedral form is not an activated process. The authors emphasize that randomly arranged isolated stacking faults will not give rise to rhombohedral reflections, only broadened hexagonal ones. The only regular arrangement that fits observation is one stacking fault on every other plane. Any other sequence must give rise to extra reflections, and these are not observed. They further conclude, on the basis that the chance of finding ten planes in the correct sequence is about 0.1%, that some ordered arrangement of dislocations occurs during deformation. Regions of rhombohedral stacking can become unobservable if just one or two dislocations glide through the stack. The work of Baker *et al.*[13] and Siems *et al.*[14] had shown that the total dislocations lying on the basal planes in graphite were always split into widely separated partial dislocations between 1000 and 2000 Å apart. This large separation means that a dislocation density of 10^{12} cm^{-2} will produce stacking faults over half the area of every layer plane. A larger density does not increase the proportion of stacking faults over a single plane. In the work under discussion the dislocation density in annealed samples was 100–1000 times smaller, and smaller still in the undeformed material.

In toto their work suggests that rhombohedral stacking

- is produced by severe basal shear;
- is around ten layers thick;
- extends over an area of around 2×10^5 unit rhombi;
- is limited to half a layer;
- is reduced by annealing, and completely removed if the temperature reaches 3000 °C;
- and can be removed by dislocation glide.

This interpretation clearly explains why isolated rhombohedral graphite cannot be produced from hexagonal graphite. There is no true allotrope—just a mosaic distribution of microcrystalline defect regions embedded in the hG host. Each defect region is, however, large enough to justify theoretical study of its structure as a quasiallotrope, and this paper has been prepared in that spirit.

III. COHESIVE ENERGY

hG and rG consist of strongly bonded graphene layers stacked under the influence of relatively weak forces in ABAB and ABCABC sequences, respectively, to use a common description. One expects their energies to be very close and this turns out to be the case. Measured stacking fault energies in hG (Refs. 13 and 14) are always positive (around 0.09 meV/atom) showing that hG is the more stable allotrope. This is confirmed by energy calculations: for example, Furthmüller *et al.* find that the cohesive energy of hG exceeds that of rG by 0.9 meV/atom.[15] This value is reduced to a mere 0.11 meV/atom, suggestively close to the stacking fault energy, in the work of Charlier *et al.*[7]

With regard to the elasticity, for which no complete calculations have yet appeared, Fahy *et al.*[16] assert: ''Because the number of bonds between the layers is the same in rhombohedral graphite and in hexagonal graphite we expect their behavior under compression to be very similar.'' The bonds between layers may be the same in number but their distributions are significantly different. The most important difference is a consequence of symmetry: in hG, where each graphene layer is a mirror plane, the internal strain is entirely confined to those layers but in rG, whose only mirror planes are normal to the layers, the internal strain is free to occur along the unique axis as well. By taking the Keating parameters for hG and transferring them to rG it is possible to make good the previous lack.

Equilibrium structure

The comment reported above that the experimental results in Ref. 8 were better served by $u=0.164$ than by the planar value $u=\frac{1}{6}$ has the implication that the planes are buckled, with atomic displacements of ±0.03 Å, a shortening of the 3.35 Å bond by 1.8%. A very simple picture, Fig. 1, explains the origin of such buckling. An eclipsed atom in hG, say 3, has equal and opposite 'large' interlayer forces acting on it due to the eclipsing atoms above and below it, similarly an uneclipsed atom, say 1, experiences equal and opposite 'small' interlayer forces due to the noneclipsing atoms above and below it. Both atoms have extremely large and balanced in-plane forces acting on them. No net forces act upwards or downwards and the integrity of the planes is ensured. Now consider those forces transferred to planar rG. No atoms are eclipsed on both sides and each atom has one large and one small interlayer force acting on it besides the very large in-plane forces. Atom 2 is drawn towards the atom below it and atom 1 towards the atom above. Small components of what were the in-plane forces will now be sufficient to augment the small forces so that together they balance the large forces. In principle this could give rise to buckled rG. However, an observable effect is unlikely: a recent *ab initio* calculation[18] of the total energy for a small range of values of u around the planar value shows a minimum for $u=0.1666$

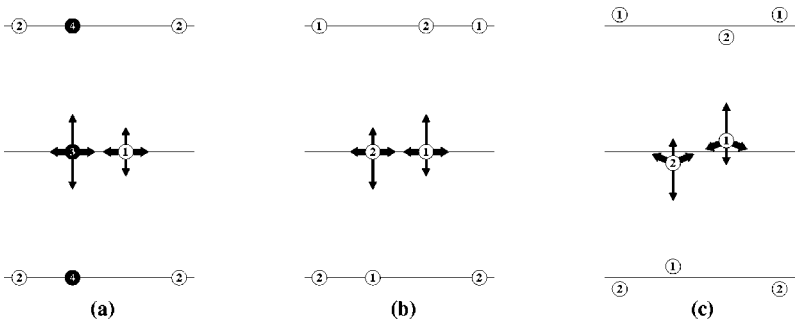

FIG. 1. Force diagram for (a) hG, (b) planar rG, and (c) buckled rG.

± 0.0003 which indicates that the net axial force on an atom is no greater than 0.2% of the in-plane force, a realistic figure consistent with the very small interlayer Keating parameters.

IV. MODIFIED KEATING MODEL

It is not in general possible to transfer force constants between different crystal structures of the same element. This is shown vividly by comparing the number and values of the parameters found for cD and hG in preceding papers.

Transferability of parameters between the diamond allotropes was possible because all atoms in both structures had the same local configuration, thereby rendering the difference in crystal structure invisible to the Keating models. The same conclusion is reached for hG and rG though with a slightly more elaborate argument. The planar configurations are identical but the interlayer configurations differ: hG has two distinct symmetric ones and rG has two identical asymmetric ones. However, the asymmetric configuration combines halves from each symmetric one and this results in identical summations in the Keating energy expressions. There is then no reason to suppose that different parameters are required by the two allotropes.

The structure of rG is fully described in Ref. 17. Two layers of it are shown in Fig. 2 and the three sets of interactions corresponding to those used for hG are indicated. Bernal notation (as used with hG) is no longer meaningful but it is useful to refer to the atoms on sublattices 1 and 2 by A and B, with superscript primes to indicate adjacent layers.

(i) The planar part of the energy per cell is the same as that in hG. The three nearest-neighbor A atoms to a B atom, see lower center portion of Fig. 2, give rise to three two-body "bond-stretching" BA_i interactions, three three-body "bond-bending" BA_i BA_j interactions, and various couplings between them. The same number of interactions arise from each A atom. Four harmonic parameters (α, β, σ, and τ) and six anharmonic parameters (γ, δ, ϵ, η, θ, and ξ) may be defined though not all of them are used.

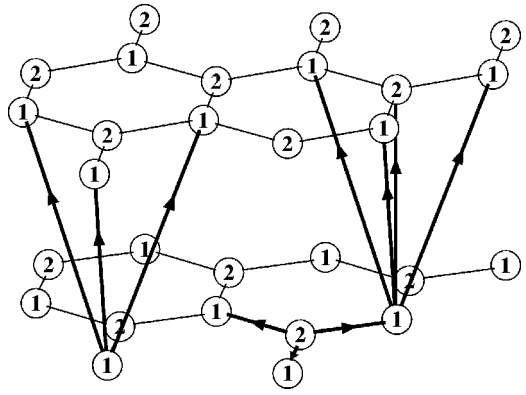

FIG. 2. Configurations of bonds in the Keating model. The interactions are described in the text.

(ii) This set comprises the two-body AB' interaction between nearest neighbors in adjacent planes, see the right-hand portion of Fig. 2, and the three-body interactions that couple AB' with the three neighboring oblique interlayer vectors AA_i'. Unlike the hG case this set is limited to the plane above. There is a corresponding set of BA' interactions confined to the plane below. Ten more parameters may be defined (with superscript $'$, corresponding to the equivalent parameters in hG).

(iii) This set comprises the three two-body AA_i' interactions and the three three-body interactions involving $AA_i'AA_j'$ pairs, see the left-hand portion of Fig. 2, together with the symmetrical group of two-body BB_i' and three-body $BB_i'BB_j'$ interactions. There is a set of each above the plane and below the plane. Ten more parameters may be defined (with superscript $''$).

In hG it was possible to ignore a potential fourth set of interactions, BB', by noting a geometrical dependence between its strains and the strains of the other three sets. Any Keating parameters associated with this set were implicitly included in the parametrization of the other sets. The corresponding case applies here through the numerous equivalences of the form $B'B=B'A+AB$. Because this is a different relation from the one in hG the implicit contribution of these interactions to the parameters above will also be different.

A. Strain variables

The strains in the modified model for rG are the same as those for cD:

$$\Delta_{ii}=2r_p^{i0}\eta_{pq}r_q^{i0}\pm 2r_p^{i0}\zeta_p+\zeta_p\zeta_p \tag{1}$$

and

$$\Delta_{ij}=2r_p^{i0}\eta_{pq}r_q^{j0}\pm(r_p^{i0}+r_p^{j0})\zeta_p+\zeta_p\zeta_p, \tag{2}$$

TABLE I. The modified Keating parameters.

	Planar			Interlayer				
	GPa Å^{-1}	eV Å^{-4}		GPa Å^{-1}	eV Å^{-4}		GPa Å^{-1}	eV Å^{-4}
α	266.21	1.6615	α'	39.55	0.2469	α''	3.231	0.02016
β	240.53	1.5013	β'	3.005	0.01875	β''	0.289	0.00180
σ	30.12	0.1880	σ'	−5.035	−0.03143			
τ	53.50	0.3340	τ'	−6.120	−0.03820	τ''	1.445	0.00902
	GPa Å^{-3}	eV Å^{-6}		MPa Å^{-3}	meV Å^{-6}		MPa Å^{-3}	meV Å^{-6}
γ	−688.00	−4.2941	γ'	197.5	1.233	γ''	−35.87	−0.2239
δ	−965.44	−6.0258						
ϵ	−366.84	−2.2896						
						ξ''	−5.44	−0.0339

where terms of order 3 and higher have been omitted. Where the sign is undetermined the + sign is taken when the reference atom lies on sublattice 1, the − when it is on 2.

B. Energy

The expressions for the modified energies per cell are the same as those for hG except that summations are now limited to two sublattices. The subscripts i and j are solely for the sake of bookkeeping—keeping in touch with the numbers of neighbors. Where, for the first time, there is only a single neighbor to consider (the AB′ interaction set) the bond has been indicated by a subscript 1.

1. Harmonic terms

The second-order energy per unit cell is

$$E^{(2)}=\tfrac{1}{2}\sum_{s=1}^{2}\sum_{i=1}^{3}\Bigg(\alpha\Delta_{ii}^2+{\sum_{j=1}^{3}}'\,[\beta\Delta_{ij}^2+\sigma(\Delta_{ii}+\Delta_{jj})\Delta_{ij}+\tau\Delta_{ii}\Delta_{jj}]+\alpha''\Delta_{ii}^2+{\sum_{j=1}^{3}}'\,[\beta''\Delta_{ij}^2+\sigma''(\Delta_{ii}+\Delta_{jj})\Delta_{ij}+\tau''\Delta_{ii}\Delta_{jj}]\Bigg)+\sum_{s=1}^{2}\Bigg(\tfrac{1}{2}\alpha'\Delta_{11}^2+\sum_{j=1}^{3}\,[\beta'\Delta_{1j}^2+\sigma'(\Delta_{11}+\Delta_{jj})\Delta_{1j}+\tau'\Delta_{11}\Delta_{jj}]\Bigg). \tag{3}$$

2. Anharmonic terms

The third-order energy per unit cell is

$$E^{(3)}=\tfrac{1}{2}\sum_{s=1}^{2}\sum_{i=1}^{3}\Bigg(\gamma\Delta_{ii}^3+{\sum_{j=1}^{3}}'\,[\delta\Delta_{ij}^3+\epsilon(\Delta_{ii}+\Delta_{jj})\Delta_{ij}^2+\eta(\Delta_{ii}^2+\Delta_{jj}^2)\Delta_{ij}+\theta\Delta_{ii}\Delta_{ij}\Delta_{jj}+\xi\Delta_{ii}\Delta_{jj}(\Delta_{ii}+\Delta_{jj})]+\gamma''\Delta_{ii}^3+{\sum_{j=1}^{3}}'\,[\delta''\Delta_{ij}^3+\epsilon''(\Delta_{ii}+\Delta_{jj})\Delta_{ij}^2+\eta''(\Delta_{ii}^2+\Delta_{jj}^2)\Delta_{ij}+\theta''\Delta_{ii}\Delta_{ij}\Delta_{jj}+\xi''\Delta_{ii}\Delta_{jj}(\Delta_{ii}+\Delta_{jj})]\Bigg)+\sum_{s=1}^{2}\Bigg(\tfrac{1}{2}\gamma'\Delta_{11}^3+\sum_{j=1}^{3}\,[\delta'\Delta_{1j}^3+\epsilon'(\Delta_{11}+\Delta_{jj})\Delta_{1j}^2+\eta'(\Delta_{11}^2+\Delta_{jj}^2)\Delta_{1j}+\theta'\Delta_{11}\Delta_{1j}\Delta_{jj}+\xi'\Delta_{11}\Delta_{jj}(\Delta_{11}+\Delta_{jj})]\Bigg). \tag{4}$$

C. Elastic constants

Expressions for the partial and inner elastic constants in terms of modified Keating parameters have been obtained for the planar rG structure by the method of homogeneous deformation. They have been listed in the Appendix. The second-order constants are presented in Table VII and the third-order ones in Table VIII. All possible parameters have been included for the sake of completeness even though only a small number of them were non-zero in the case of hG. Comparison with Tables IX, X, and XI in Ref. 3 shows that all the partial constants have the same expressions in both graphite allotropes. The most notable difference is the lack of any contribution to the inner elastic constants from the next-nearest-neighbor (NNN) interlayer interactions. This is because the AA′ (and BB′) connect points on the same sublattice. At the third order five of the six D_{iJK} that involve ξ' will be zero because the transferred parameters do not include it.

TABLE II. Calculated second- and third-order partial and inner elastic constants. Units are GPa for $C^0_{IJ.}$, GPa Å^{-1} for $D_{iJ.}$, GPa Å^{-2} for $E_{ij.}$, and GPa Å^{-3} for F_{ijk}.

Partial		Inner		Partial		Inner			
C^0_{11}	1063.85	D_{16}	39.5	C^0_{111}	−8641.4	D_{136}	0.	E_{111}	−9161
C^0_{12}	176.15	D_{15}	−4.7	C^0_{113}	−14.1	D_{145}	0.	E_{112}	2139
C^0_{13}	7.9	D_{31}	−39.9	C^0_{133}	−120.0	D_{211}	12 524	E_{113}	31.1
C^0_{33}	36.5	D_{33}	−0.04	C^0_{333}	−572.0	D_{222}	−10 879	E_{135}	0.
C^0_{44}	5.05			C^0_{144}	−4.4	D_{314}	0.	E_{331}	216.1
C^0_{14}	1.6	E_{11}	502.8	C^0_{244}	−9.1	D_{311}	0.	E_{333}	99.1
		E_{33}	148.0	C^0_{344}	−74.7	D_{312}	0.		
				C^0_{166}	−5887.0	D_{313}	0.		
				C^0_{266}	2046.7	D_{333}	227.8		
				C^0_{366}	−3.4	D_{344}	0	F_{112}	1547
				C^0_{114}	−2.4			F_{113}	48.8
				C^0_{124}	−0.5			F_{333}	166.8
				C^0_{134}	−15.8				
				C^0_{444}	11.0				

The partial and inner elastic constants derived from Tables VII and VIII using values from Table I, and checked by a homogeneous deformation calculation,[19] are shown in Table II. The large number of null D_{iJK} and E_{ijK} components is a pseudosymmetry effect arising from the limited number of interactions taken in the model combined with the assumption of planar layers. A similar effect was seen in hD[1] when the lattice parameters were chosen to give the quasi-cD configuration: the linear compressibility became isotropic. A new feature is the appearance of additional anharmonic contributions, $F^{(2)}_{113}$ and $F^{(2)}_{333}$, to the harmonic energy.

When the pseudosymmetry is broken by the buckling of layers then u is no longer $\frac{1}{6}$, but smaller, and many coefficients that are zero (i.e., blank spaces) in Tables VII and VIII will become nonzero, as will the associated constants.

The internal strain component common to the two allotropes is slightly different, as shown in Table III, and the null value for A_{33} is another pseudosymmetry consequence.

The full decomposition of the constants is given in Table IV. The overall picture reveals that the two graphite allotropes are remarkably similar. The calculated values of C_{11} and C_{12} in rG are a little smaller than they are in hG on account of the extra contributions of internal strain and this in turn makes k_a a little bigger than it is in hG. At the third order it is only C_{133} that is greatly changed by internal strain, but this gives S_{133} the value -39.5 TPa^{-2} whereas it is

TABLE III. The internal strain tensors in Å. The values for rG appear on the left. The actual in-plane internal strain in hG is shown on the right for comparison.

iJ	A_{iJ}	$A^2_{iJ}+A^3_{iJ}$
16	−0.079	−0.083
15	0.009	
31	0.269	
33	0.0	

TABLE IV. The composition of the calculated elastic stiffnesses, and the corresponding compliances and compressibilities. Stiffnesses are in GPa, second-order compliances in TPa^{-1} and third-order compliances in TPa^{-2}.

	← $C_{IJ.}$ →			$S_{IJ.}$
$IJ.$	Partial	Internal	Total	Total
11	1063.85	−13.86	1049.99	0.980
12	176.15	−7.64	168.51	−0.157
13	7.90	−0.01	7.89	−0.178
33	36.5	0.0	36.5	27.47
44	5.05	−0.04	5.01	200.1
14	1.56	0.37	1.93	−0.438
			k_a	0.645
			k_c	27.1
			k_v	28.4
111	−8641.4	−2863.4	−11 504.8	7.36
113	−14.2	7.4	−6.7	−2.81
133	−120.0	61.4	−58.6	−39.5
333	−572.0	0.2	−571.8	11 809.9
144	−4.4	0.2	−4.2	−221.7
244	−9.1	−0.8	−9.9	−342.0
344	−74.7	0.0	−74.7	81 921.7
166	−5887.1	−853.4	−6740.5	35.1
266	2046.7	−1030.2	1016.5	−10.4
366	−3.4	0.2	−3.2	−5.1
114	−2.4	113.6	111.2	−21.0
124	−0.5	0.7	0.2	−4.6
134	−15.8	−0.1	−15.9	−74.8
444	11.0	0.0	11.0	−88 123.3
			K_a	−30.5
			K_c	11 646
			K_v	11 585

TABLE V. Pressure derivatives of the second-order stiffnesses compared with target data for hG.

	C'_{11}	C'_{12}	C'_{13}	C'_{33}	C'_{44}	C'_{14}
rG	38.8	10.9	3.1	12.7	1.9	0.4
hG target	39.0	11.0	3.1	14.6	1.9	

-1.4 TPa^{-2} in hG. This causes the one upset in the fitting: it produces a negative K_a. This was the most difficult target to fit in hG because, as explained in Ref. 2, it depends on the *interlayer* anharmonicity and particularly on the smallness of S_{133} relative to S_{333}. The remaining compressibilities k_c, K_c, k_v, and K_v are effectively identical in the two allotropes.

The pressure derivatives of the second-order constants are shown in Table V. The first five are essentially the same as the fitted values of the anharmonic targets for hG.

D. Zone-center optic modes

The E_g mode in rG mimics the E_{2g2} mode of hG with a frequency of 47.43 THz and a pressure derivative of 0.142 THz/GPa. Likewise the A_{1g} mode mimics the B_{1g2} with values of 25.74 THz and -0.96 THz/GPa. The behavior under pressure is shown in Fig. 3 and indicates a phase transition at about 21.7 GPa.

V. RG-TO-CD TRANSFORMATION

Although rG has never been isolated this has not inhibited study of its possible conversion to cD. A continuous transformation between the two structures can be envisaged because cD can be described by a primitive rhombohedral cell with two atoms in the basis in just the same way as rG. The quasi-rD picture is illustrated in Ref. 17. The top two rows of Table VI show the lattice parameters (of the triple hexagonal cell), the volume (of the primitive rhombohedral cell), and the atomic position parameters of the two structures involved. Also listed are the lengths of the axial bonds R, the nonaxial bonds r, and the buckling angle θ. These latter parameters, indicated in Fig. 4, are related to the former by

$$R=2uc, \tag{5}$$

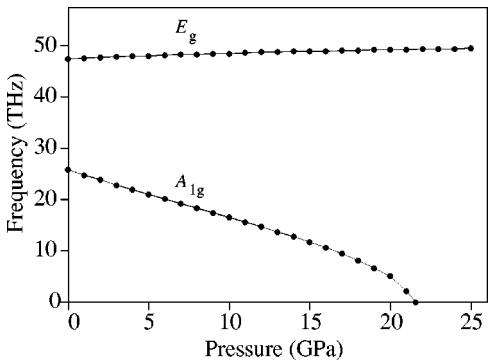

FIG. 3. Pressure dependence of the zone-center frequencies.

$$r\cos\theta=2c\left(u-\frac{1}{6}\right), \tag{6}$$

and

$$r\sin\theta=\frac{a}{\sqrt{3}}. \tag{7}$$

The volume per pair of atoms is

$$V_c=\frac{\sqrt{3}}{6}ca^2. \tag{8}$$

R, r, and θ all change continuously during such a transformation and there is no uniquely constrained path. From a purely geometrical viewpoint the values of a, c, and u may be interpolated uniformly between their extreme values and R, r, and θ calculated by the equations above. This would be to ignore the physics, though, particularly the internal strain. Two physical approaches have been developed: one involving energy minimization, the other enthalpy minimization along a hydrostatic compression path. These are described briefly below, accompanied by complementary deductions using the Keating model.

A. Energy-minimization calculations

In Ref. 5 Kertesz and Hoffmann presented an orbital model for this solid-state, high-pressure, transformation, relating it to chemical reactions having orbital symmetry constraints. They took R as the independent reaction coordinate and optimized r and θ at each value using extended Hückel band calculations. They identified a transition state at the maximum of the total energy versus R curve. This occurred

TABLE VI. End points and transition-state parameters.

	a	c	V_c	u	R	r	θ
rG	2.460	10.048	17.554	$\frac{1}{6}$	3.350	1.420	90.00
cD	2.522	6.178	11.346	$\frac{1}{8}$	1.545	1.545	109.47
Ref. 5	2.519	6.684	12.243	0.139	1.86	1.50	104.2
Ref. 6(1)	2.513	7.088	12.920	0.182	2.07	1.48	101.4
Geometrical path	2.504	6.810	12.304	0.140	1.91	1.49	104.0
Ref. 6(2)	2.372	6.770	11.0	0.155	2.1	1.38	97.0
Compression path	2.435	6.488	11.1	0.152	1.97	1.42	97.8

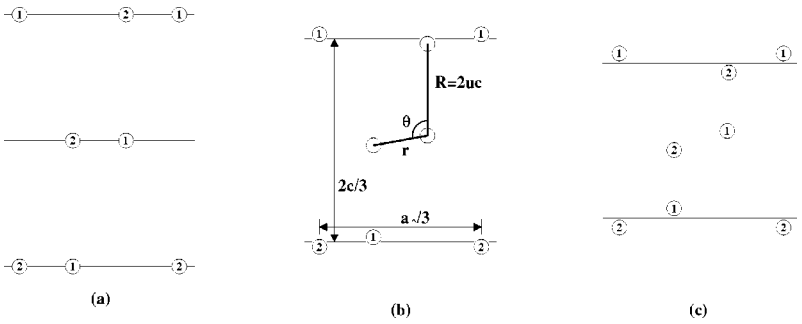

FIG. 4. rG-to-cD transformation path (a) initial rG, (b) intermediate stage, showing the essential parameters, and (c) final cD.

at $R=1.86$ Å, $r=1.5$ Å, and $\theta=104.2°$. The energy barrier E_B was about 0.6 eV/atom. The transition state therefore occurs when $a=2.519$ Å, $c=6.684$ Å, and $u=0.139$. These results have been entered in the third row of Table VI.

They used the small initial rate of increase of r with R to argue that the graphene layers do not buckle at low pressure. In connection with the (unstable) transition state they remark that it is customary to relate different solid-state structures by studies of hypothetical, sometimes unstable, structural models.

Fahy, Louie, and Cohen[6] subsequently made a pseudopotential total-energy study of the transformation. In the first of two calculations they followed the rationale of the above work and found an energy barrier of 0.33 eV/atom when $R=2.07$ Å, $r=1.48$ Å, and $\theta=101.4°$. This result has been entered in row 4 of Table VI. In this study they followed the charge density in the plane of Fig. 4(b) along the energy-minimizing path. They concluded, first, that only when $R<2.1$ Å did the charge density between the layers become substantially inhomogeneous and accumulate along the axial bond and, second, that not until $R<1.8$ Å did the double peak, characteristic of the sp^3 bond in cD, appear.

These observations have been used to provide limits in the algorithm that handles the merging of the cD and rG parametrizations. The Keating energy is taken as

$$E=fE_{rG}+(1-f)E_{cD}, \tag{9}$$

where, with $R_{\min}=1.8$ and $R_{\max}=2.1$, the switching function is

$$f=\begin{cases} 0 & \text{for } R<R_{\min}, \\ \dfrac{1}{2}-\dfrac{1}{2}\cos\left(\dfrac{\pi(R-R_{\min})}{R_{\max}-R_{\min}}\right) & \text{for } R_{\min}\leqslant R\leqslant R_{\max}, \\ 1 & \text{for } R_{\max}<R. \end{cases} \tag{10}$$

In the following illustration c, a^2, and uc are interpolated uniformly between their extremes. This procedure has the effect of making the initial variation of a small, in keeping with the anisotropy of the linear compressibilities. As both c and uc are changed proportionately the variation of u itself is also small initially: buckling is therefore slow to start, as found in the studies under discussion. The results for the second-order elastic constants are illustrated in Fig. 5, for the internal strain parameters in Fig. 6 and for the zone-center optic-mode frequencies in Fig. 7. Each display is divided into 3 by the upper and lower limits of the switching function. On the left only the rG parameters are involved, any variations being due solely to the changes in the geometry of the cell, and on the right only cD parameters are involved. The mixing of the two régimes occurs in between.

It is partly the geometrical aspect of the partial constants, the disposition of a and d in the common factors in Table VII, and partly the internal strain that determines the overall variation of the total constants seen in the rG region. Thus both C_{11}^0 and C_{12}^0, which vary as a^2/d, increase in size by 44% across the rG region. Roughly equal contributions from inner displacement are subtracted from each, about 5% of C_{11}^0 but 25% of C_{12}^0 at the limit, leaving the variation of C_{11} to dominate the picture. The only other feature that merits comment is the variation of C_{13}: this very small constant makes a negative excursion in the rG region and then,

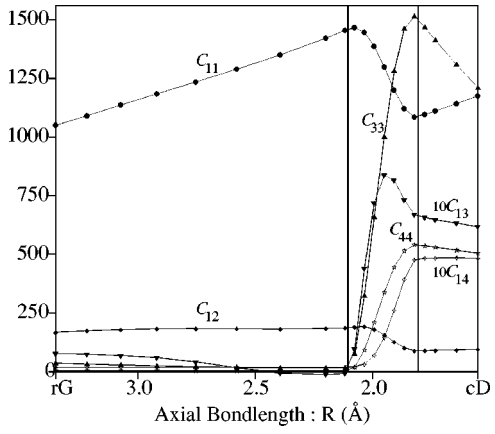

FIG. 5. Second-order elastic constants along a transformation path. C_{13} and C_{14} are shown at $\times 10$ magnification. Terminal values on the right are quasi-rD values.

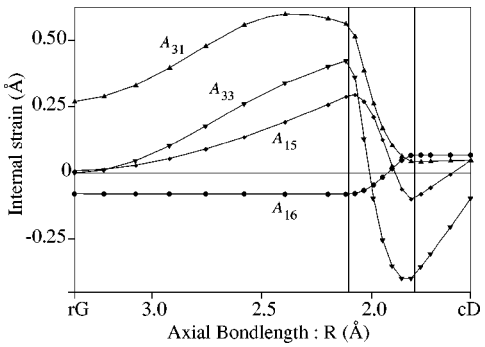

FIG. 6. Internal strain parameters along a transformation path. Terminal values on the right are quasi-rD values.

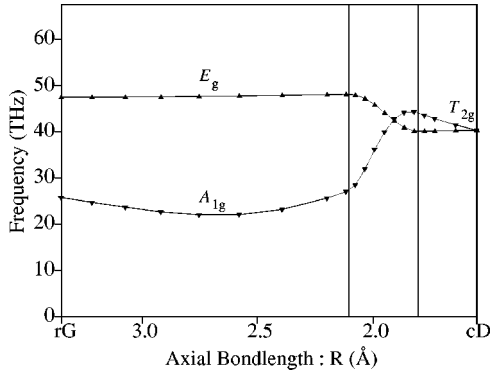

FIG. 7. Zone-center frequencies along a transformation path. The terminal value on the right is the quasi-rD value.

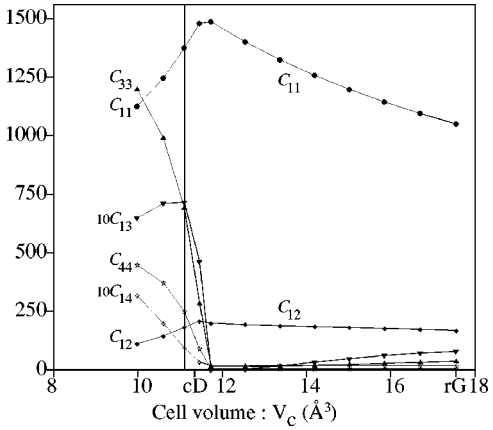

FIG. 8. Second-order elastic constants along a hydrostatic compression path. C_{13} and C_{14} are shown at $\times 10$ magnification. The vertical line marks the state where u and θ are extremal.

uniquely, rises to a maximum in the middle of the transition region. The significance of this is not clear. The apparent constancy of $A_{16}(=-D_{16}/E_{11})$ is due to its net common factor of a which increases by only 1.4% across the rG region.

The one interesting feature of the optic-mode frequencies is their degeneracy in the transition region at $R=1.9$ Å, close to the value at which the onset of peaks in the electron density along the axial bond occurs[6] and reasonably close to the value 1.76 Å, deducible from measurements on Fig. 3 in Ref. 5, where a symmetry imposed level crossing at the Γ point occurs. The latter is related to the change from sp^2+p_z to sp^3 bonding, essentially the same fact. The data for the present transition point have been added to Table VI for comparison.

B. Hydrostatic compression path

Fahy, Louie, and Cohen's second calculation followed a hydrostatic pressure path. The cell volume V_c was interpolated between its extremes and extrapolated beyond. The associated enthalpy, $E+pV_c$, at each point was minimized. The results were very different from those based on energy minimization. The path for example does not lead continuously to the cD structure but terminates when $p=80$ GPa and $V_c=11.0$ Å^3 at which point $R=2.1$ Å, $r=1.38$ Å, and $\theta=97°$. This result has been entered in row five of Table VI.

The compression path is simulated here by stepping c uniformly in 4% increments of the difference between its extreme values. From the initially uncompressed rG the pressure increment required to drive the structure to the next state is deduced from $\Delta c/c=-k_c p+\frac{1}{2}(K_c-k_c^2)p^2$, the corresponding increment in a from $\Delta a/a=-k_a p+\frac{1}{2}(K_a-k_a^2)p^2$ and the (purely axial) increment in R from $\Delta R=-p(2A_{31}k_a+A_{33}k_c)$. Over the rG region the pressure increments are small, starting at 0.65 GPa and dropping to 0.4

TABLE VII. Coefficients of the modified Keating parameters in the second-order partial and inner elastic constants. The common factors are expressed in terms of the lattice parameter a and the interlayer spacing d, with t standing for $\sqrt{3}$.

		Planar				Interlayer: NN				Interlayer: NNN			
	Factor	α	β	σ	τ	α'	β'	σ'	τ'	α''	β''	σ''	τ''
C_{11}^0	$2ta^2/3d$	1	1	−2	1					2	2	−4	2
C_{12}^0	$2ta^2/9d$	1	−1	−2	5					2	−2	−4	10
C_{13}^0	$4td/3$							2	2	4	−4	4	8
C_{33}^0	$16td^3/a^2$					$\frac{1}{3}$	2	4	2	2	4	8	4
C_{44}^0	$4td/3$						1	2		4	2	4	−4
C_{14}^0	$2a/3$							1		4	−4	−2	−4
D_{16}	$2a/3d$	−2	2	1	2			1					
D_{15}	$4t/3$						1	1					
D_{31}	$4t/3$							1	2				
D_{33}	$16td^2/3a^2$					1	3	6	3				
E_{11}	$4t/3d$	2	1	2	−2		1						
E_{33}	$8td/3a^2$					2	3	6					
$E^{(2)}_{111,112,331}$	$8t/3d$	1	−1	1	2				1				
$E^{(2)}_{113,333}$	$16td/3a^2$					1		3	3				
$F^{(2)}_{113}$	$8t/3a^2$					2		3					
$F^{(2)}_{333}$	$8t/a^2$					2		3					

TABLE VIII. Coefficients of the modified Keating parameters in the third-order partial elastic constants and inner elastic constants. Common factors expressed as in Table VII.

		Planar						Interlayer: NN						Interlayer: NNN					
	Factor	γ	δ	ϵ	η	θ	ξ	γ'	δ'	ϵ'	η'	θ'	ξ'	γ''	δ''	ϵ''	η''	θ''	ξ''
C^0_{111}	ta^4/d	1	−1	2	−2	−1	2							2	−2	4	−4	−2	4
C^0_{113}	$8ta^2d/3$										1		1	3	3	−2		−1	8
C_{133}	$32td^3/3$									1	2	1	3	3	−3		6	3	12
C_{333}	$32td^5/a^2$							1	6	12	12	6	12	6	12	24	24	12	24
C^0_{144}	$2ta^2d/9$									1	4			12	−12	−6		12	24
C^0_{244}	$2ta^2d/3$									1	4			12		2		4	−8
C_{344}	$8td^3/3$								3	6	8	2	4	12	6	12	24		
C^0_{166}	$ta^4/9d$	3		2	−6	1	−2							6		4	−12	2	−4
C^0_{266}	$ta^4/9d$	1	−4	6	−2	−3	2							2	−8	12	−4	−6	4
C^0_{366}	$8ta^2d/9$										1		1	3	6			−3	
C^0_{114}	$2a^3/3$										1			6	6	−4	−6	−2	4
C^0_{124}	$2a^3/9$										1			6	−6		−6	6	−12
C^0_{134}	$4ad^2/3$									2	6	1	4	12	−12	−12	12	−6	
C^0_{444}	$2ad^2$								−1	−2	−4			−8	2	4	−8	8	16
D_{136}	$2ad/3$									4	4	2							
D_{145}	$2ad/3$								3	4	4								
D_{211}	$2a^3/3d$	−3	−3	2	3	1	−2				1								
D_{222}	$2a^3/3d$	5	1	−2	−5	1	−2				$-\frac{5}{3}$								
D_{314}	$4ad/3$									1	2	1	4						
D_{311}	$4ta^2/3$										1		2						
D_{312}	$4ta^2/9$										1		2						
D_{313}	$8td^2/3$									2	2	3	8						
D_{333}	$32td^4/a^2$							1	3	6	6	3	6						
D_{344}	$4td^2/3$								3	6	4	4	8						
$E^{(3)}_{111}$	$2ta^2/3d$	6		1		2	−4			1									
$E^{(3)}_{112}$	$2ta^2/9d$	6	−6	−3		6	12			1									
$E^{(3)}_{113}$	$8td/3$								3	2									
$E^{(3)}_{135}$	$16td/3$								3	4		2							
$E^{(3)}_{114}$	$2a/3$								3	2									
$E^{(3)}_{136}$	$2a/3$									2		2							
$E^{(3)}_{331}$	$8td/3$									1		2	4						
$E^{(3)}_{333}$	$16td^3/a^2$							2	3	6	8	2	4						
$F^{(3)}_{112}$	$2a/d$	−4	1	2	−4	4	8		1										
$F^{(3)}_{113}$	$t/3$								12	8									
$F^{(3)}_{333}$	$8td^2/a^2$							4	3	6	12								

GPa, and accumulate to 9.6 GPa. As soon as R falls below 2.1 Å, however, the steep reductions in axial compressibilities mean that very large pressure increments, 9 GPa and escalating, are needed to generate successive states. The variation of the elastic constants is shown in Fig. 8 as a function of cell volume V_c for ease of comparison with the results in Ref. 6. The path is traversed from right to left. The vertical line indicates the state at which u and θ are extremal: it occurs when $p=19.1$ GPa, $V_c=11.1$ Å^3, $u=0.152$, and $\theta=97.8°$. These parameters have been added to Table VI. Apart from the pressure these parameters are close to those of the metastable state identified in Ref. 6. The pressure itself is close to the critical value 21.7 GPa indicated by the pressure dependence of the A_{1g} mode frequency. To the left of this line the structure becomes more graphitic. The state at the extreme left has the c value of cD and is attained at a pressure of 72.6 GPa. It is remarkably similar to cD elastically: the bulk modulus is 1.8% down, the axial modulus just

0.3% down. The bond configuration, though, is a highly distorted tetrahedron in which $R=1.88$ Å, $r=1.38$ Å, and $\theta=97.5°$.

C. Other paths

A triaxial step-by-step process has been studied in which equal positive stress increments σ_1 and σ_2 stretch the basal plane at the same time as a negative increment σ_3 squashes the planes together. The procedure leads to the cD cell parameters in 100 steps but is less successful than the hydrostatic procedure in attaining a cD atomic configuration. The stretching of the basal plane inhibits buckling of the layers and the parameter u never drops below 0.161.

The single reason that such processes cannot lead from rG to cD is the phenomenon of internal strain. The relative compression of the axial bond R does not keep pace with the relative compression of the cell parameter c because relative displacement of sublattices will always occur to minimize the deformation energy.

The best practical route to an rG-to-cD conversion is probably that of uniaxial stress. A compressive stress σ_3 changes the lattice parameters according to

$$\Delta a/a = S_{13}\sigma_3 + \tfrac{1}{2}S_{133}\sigma_3^2 \tag{11}$$

and

$$\Delta c/c = S_{33}\sigma_3 + \tfrac{1}{2}S_{333}\sigma_3^2. \tag{12}$$

Since $S_{13}<0$ and $S_{33}>0$ the compressive stress (which is negative) causes a to increase and c to decrease simultaneously.

It may be that all these approaches are of academic interest only. In a molecular-dynamics simulation of the conversion by Scandolo *et al.*[20] it was found that hG was converted into both cD and hD *via* an intermediate orthorhombic phase of graphite. This process resulted in different orientation relationships between the initial and final crystal structures from the one implicit in the discussions above. Although rG was not explicitly studied it seems likely that it will behave in a similar way.

VI. SUMMARY

This paper began with a discussion of the precise nature of rhombohedral graphite, focusing on the initial structural studies of natural graphite and work on defects to be seen therein. It was concluded that the rhombohedral form was not a true allotrope but a mosaic distribution of microcrystalline defect regions embedded in the hG host. These regions could be sufficiently large, however, to merit their study as if they were truly allotropic. The issue of whether the equilibrium state consisted of planar or buckled layers was resolved in favor of planar layers.

The elasticity in terms of the modified Keating model was then calculated for the planar structure. The transfer of Keating parameters from hG to rG showed that the two allotropes were elastically extremely similar, apart from the negative anharmonic in-plane compressibility K_a. The possession of a set of elastic constants for this as-yet-uncharacterized material provided an opportunity to explore the rG-to-cD transformation in greater detail.

VII. MODIFIED KEATING MODEL: SCOPE FOR FURTHER APPLICATION

The successful use of the modified Keating model with hG suggests that the model will be well suited to studying the elasticity and the vibrational properties of nanotubes and fullerenes. As previously the model can be used in conjunction with specific interatomic potentials if that appears appropriate—to handle the Coulomb interaction in an ionic solid, for example. In such cases a first-order Keating energy has to be introduced to balance the first-order part of the additional potential and to annul the first-order elastic constants that arise.

Further possible synoptic studies of cases where a particular structural motif underlies a variety of crystal structures spring to mind: SiO_2 units in quartzes, tridymites, cristobalites, coesite, and stishovite; H_2O in various ices (in IceI the O atoms occupy a quasi-hD configuration) and BN in its zinc-blende, wurtzite, and graphitic versions. Rationalization of data via the modified Keating model may also serve as a useful preliminary in the derivation of a more sophisticated transferable interatomic potential.

APPENDIX: ELASTIC CONSTANTS IN THE MODIFIED KEATING MODEL

Each constant M_i is written as a linear combination of Keating parameters K_j with coefficients μ_j and a common factor F_i: $M_i = F_i \times \Sigma \mu_j K_j$. The second-order constants appear in Table VII and the third-order ones in Table VIII. The common factors in these Tables have been expressed in terms of the interlayer spacing d rather than the lattice parameter c to facilitate comparison with the treatment of hG in Ref. 3.

[1] C. S. G. Cousins, Phys. Rev. B **67**, 024108 (2003).
[2] C. S. G. Cousins, Phys. Rev. B **67**, 024107 (2003).
[3] C. S. G. Cousins and M. I. Heggie, Phys. Rev. B **67**, 024109 (2003).
[4] R. R. Haering, Can. J. Phys. **36**, 352 (1958).
[5] M. Kertesz and R. Hoffmann, J. Solid State Chem. **54**, 313 (1984).
[6] S. Fahy, S. G. Louie, and M. L. Cohen, Phys. Rev. B **34**, 1191 (1986).
[7] J.-C. Charlier, X. Gonze, and J.-P. Michenaud, Carbon **32**, 289 (1994).
[8] H. Lipson and A. R. Stokes, Proc. R. Soc. London, Ser. A **181**, 101 (1942).
[9] J. D. Bernal, Proc. R. Soc. London, Ser. A **106**, 749 (1924).

[10] O. Hassel and H. Mark, Z. Phys. **25**, 317 (2924).
[11] H. Ott, Ann. Phys. (Leipzig) **85**, 81 (1928).
[12] E. J. Freise and A. Kelly, Philos. Mag. **8**, 1519 (1963).
[13] C. Baker, Y. T. Chou, and A. Kelly, Philos. Mag. **6**, 1305 (1961).
[14] R. Siems, S. Amelinckx, and P. Delavignette, Z. Phys. **165**, 502 (1961).
[15] J. Furthmüller, J. Hafner, and G. Kresse, Phys. Rev. B **50**, 15 606 (1994).
[16] S. Fahy, S. G. Louie, and M. L. Cohen, Phys. Rev. B **35**, 7623 (1987).
[17] C. S. G. Cousins, J. Phys.: Condens. Matter **14**, 5091 (2002).
[18] I am most grateful to G. P. Srivastava for making these calculations on my behalf (unpublished).
[19] C. S. G. Cousins, J. Phys.: Condens. Matter **14**, 5115 (2002).
[20] S. Scandolo, M. Bernasconi, G. L. Chiarotti, P. Focher, and E. Tosatti, Phys. Rev. Lett. **74**, 4015 (1995).